

Multiple-scale analysis on the radiation within the nonlinearly coupled KdV equations

Yezheng Li¹, Joseph A. Biello², Yerong Li³

¹ Applied Mathematics and Computational Science, University of Pennsylvania, David Rittenhouse Laboratory, 209 South 33rd Street, Philadelphia, PA 19104.

² Department of Mathematics, University of California, Davis, CA 95616.

³ Department of Applied Physics and Materials Science, California Institute of Technology, Pasadena, CA 91125, USA

E-mail: yezheng@sas.upenn.edu, biello@math.ucdavis.edu, yerong.li@caltech.edu

Abstract. A multiple scale model of the nonlinearly coupled KdV equations is established to predict mechanism of interaction of equatorial Rossby waves and barotropic waves in certain case. Analytically, predicted precursor radiation is a centrosymmetric object and is shown in excellent quantitative agreement with numerical simulations; furthermore, the multiple scale model elucidates the salient mechanisms of the interaction of solitary waves and the mechanism for radiation. While the atmosphere-ocean science community is very interested in theoretical studies of tropical wave interactions and in developing reduced dynamical models that can explain some key features of equatorial phenomena, our analytic predictions quantitatively explain formation of radiation during interaction in Biello's model beyond qualitative level.

PACS numbers: 91.10.Vr

AMS classification scheme numbers: 35B40

Keywords: "precursor" radiation, multiple scale analysis, fast-slow decomposition

Submitted to: *Nonlinearity*

1. Introduction

1.1. Atmospheric background and solitary structures

Some poorly understood phenomena in atmosphere-ocean science involve a complex nonlinear interaction of clouds, moisture, and convection on a large variety of scales in both time and space, ranging from cumulus clouds over a few kilometers to intraseasonal oscillations over planetary scales of order 40,000 km [1–4]. While current numerical simulations still fail to capture mechanism of interaction on multiple scales [1, 3, 5], ocean-atmosphere science community is interested in theoretical studies of tropical wave interactions and in developing reduced dynamical models that can at least qualitatively explain some key features of equatorial phenomena [1–3, 5–9].

Under this circumstance, amplitude equations describing the interaction of equatorial Rossby waves and barotropic waves

$$a_t - (1 - 2\gamma)a_{xxx} + (ab)_x = 0, \quad (1)$$

$$b_t - b_{xxx} + \left(\frac{a^2}{2}\right)_x = 0, \quad (2)$$

are derived by Biello and Majda [6, 7] and are used as a model for long range interactions (teleconnections) between the tropical and midlatitude troposphere. On one hand, assessing the accuracy of this low-dimensional model (amongst the many) of the tropical atmosphere that take advantage of equatorial long-wave theory [7, 10, 11] is an important ongoing task [12–14]; on the other hand, different from some test models without instability nor positive Lyapunov exponents [15], this simplified quasi-equilibrium tropical model (2) is more realistic achieved by allowing active barotropic dynamics and coupled nonlinear advection which allows for tropical-extratropical wave interactions [6, 7, 15–17].

[6, 18] also explore solitary structures (which are not rare in atmospheric science) within these amplitude equations (2) which may explain transfer of energy between waves. The nonlinearly coupled KdV equations

$$\begin{aligned} u_t - (1 - \gamma)u_{xxx} + uu_x &= \gamma v_{xxx} + \frac{(uv)_x}{2}, \\ v_t - (1 - \gamma)v_{xxx} + vv_x &= \gamma u_{xxx} + \frac{(uv)_x}{2}. \end{aligned}$$

are actually recast by a linear transformation from these amplitude equations (2) [18]. u, v govern the amplitude of two types of modes, each of which consists of a coupled tropical/midlatitude flow. We choose to work with $\gamma = 0$

$$\begin{aligned} u_t - u_{xxx} + uu_x &= \frac{(uv)_x}{2}, \\ v_t - v_{xxx} + vv_x &= \frac{(uv)_x}{2}. \end{aligned} \quad (3)$$

due to the generic nature of the interaction [18].

Despite the need to understand its role in atmospheric background [15, 19–21], analysis of solitons' behavior is very incomplete and it is precisely at the point of solitary

waves that interesting dynamics arise [6]. Notice $u \equiv 0$ or $v \equiv 0$ are invariant subspaces of (3) with the non-zero function evolving according to the KdV equation [18]; take $v \equiv 0$ as an example, KdV solution includes

$$u(x, t) = \epsilon^{-2} K(\epsilon^{-1}(x - c\epsilon^{-2}t)), \quad K(\xi) = -12 \operatorname{sech}^2 \xi, \quad c = -4.$$

and $c\epsilon^{-2}$ is the traveling velocity of the soliton. Inspired by these solitary structures, Biello [18] presents numerical results showing the collision of one u -soliton with one v -soliton initialized by

$$u(x, 0) = K(x), \quad v(x, 0) = \epsilon^{-2} K(\epsilon^{-1}(x - x_v^0)), \quad (4)$$

but only with relatively large $\epsilon = 0.75$. Indeed, two solitons remain their solitary form before they come close to each other and interaction happens later on even though such initialization is well-posed due to work [22–24]. Just by numerical simulation majorly with $\epsilon = 0.75$, Biello [18] is sharp enough to insinuate some details of the interaction including shears, a small amount of rightward traveling radiation generated, etc., and a broad range of interesting and unexplained behavior is displayed in just few numerical examples [18]. As a typical phenomenon in the simulation, the transversely narrow and sharply peaked soliton shape results in an eye-catching but small scale centrosymmetric precursor radiation in v . Such a peak has been observed experimentally in figure 6 and provides a possible mechanism for the formation of shear and radiation show in figure 4,6; [18] also presents analogous shear, peak, radiation.

1.2. Multiple-scale model and approximation results

In this paper, we focus on the case of $\epsilon \rightarrow 0$ in (4). Notably, numerical simulation of solitary interaction is both our start and our end for solitons' behavior studying. Speaking of simulations, radiations during and after interaction of solitons pose a particular difficulty for theoretical investigation and numerical simulations of solitary waves representing "soliton amplitudes". Eventually, we successfully apply multiple-scale model to analytically predict radiations, interaction (with $\epsilon \rightarrow 0$):

(i) the ansatz of multiple scale model is

$$\begin{aligned} u(x, \epsilon^{-1}x, \epsilon^{-3}t) &= U^0(x) + U^F(x, \epsilon^{-1}x, \epsilon^{-3}t) \\ &\quad + \epsilon U^B(x, \epsilon^{-1}x, \epsilon^{-3}t) + o(\epsilon), \\ v(x, \epsilon^{-1}x, \epsilon^{-3}t) &= \epsilon^{-2} V^0(\epsilon^{-1}x, \epsilon^{-3}t) + V^F(x, \epsilon^{-1}x, \epsilon^{-3}t) \\ &\quad + \epsilon V^R(x, \epsilon^{-1}x, \epsilon^{-3}t) + o(\epsilon); \end{aligned}$$

where we have two scales in space and a single scale in time; or alternatively

$$\begin{aligned} u(x, X, T) &= U^0(x) + U^F(x, X, T) + \epsilon U^B(x, X, T) + o(\epsilon), \\ v(x, X, T) &= \epsilon^{-2} V^0(X, T) + V^F(x, X, T) + \epsilon V^R(x, X, T) + o(\epsilon). \end{aligned} \quad (5)$$

where small space scale is $X = \epsilon^{-1}x$ and the single time scale is $T = \epsilon^{-3}t$ (fast time).

U^0 is the base of wave u and V^0 is approximately the original sharp soliton of wave v . U^F (figure 1) is fleeting solitary structure inside wave u while (inconspicuous) V^F is the counterpart for wave v . ϵV^R is precursor v radiation (figure 2, 6), one of our focuses of attention while (less important and obscure as well) ϵU^B is the bruise left on u after the interaction.

- (ii) the model captures mechanism (three phases of interaction) for the formation of shear and radiation:

precursor v -radiation is formed firstly; then it interacts with u , forming u -radiation and v -radiation in-situ.

- (iii) the precursor v radiation (after the interaction) is of the form

$$\epsilon V^R(x, X, T) = \epsilon C_V^R R(x), \text{ as } T \rightarrow \infty, \quad (6)$$

where normalized $R(x) = \frac{3\sqrt{3}}{2} \sinh(x) \cosh^3(x)$ and C_V^R is a positive constant representing height of V^R : $C_V^R = 1.03 \sim 1.14$ from simulation (figure 2,6,7; table 2) and our WKB model predicts $C_V^R = 4.11$ (second part of figure 10; table 2; derivation in (C.2)). By comparison, our WKB model's prediction of less important U^B agrees extremely well with numerical simulations with $C_U^B = -15.37$ (figure 4,8, first part of figure 10; table 1; derivation in (C.1)) within $\epsilon U^B(x, X, T) = \epsilon C_U^B R(x)$, as $T \rightarrow \infty$.

1.3. Outline of solution strategy

The objective of this work is to use multiple scale model to predict "precursor" radiation ϵV^R (figure 2,6) as $\epsilon \rightarrow 0$ in (3,4). Our analytical strategy has a few key steps which exploit the multi-scale structure observed from numerical simulations. Our steps will proceed as follows:

- (i) We present in section 1.4 numerical simulations to better describe the interaction we are to analyse. Simulations also motivate two important tools for asymptotic analysis – multiple scale ansatz and fast-slow decomposition.
- (ii) Motivated by simulations, we present in section 2.1 our multiple scale model to predict ϵV^R , "precursor" radiation of v . Connections to its numerical motivations (section 1.4) are indispensably focused.
- (iii) Also motivated by simulations, we mathematically clarify in section 2.2 the fast-slow decomposition. Connections to their numerical motivations (section 1.4) are indispensably focused. This allows us to solve equations arisen in WKB theory by reducing PDEs to ODEs.
- (iv) Equipped with the multiple-scale model and fast-slow decomposition, we are able, in section 2.3, to predict the simple analytic solution for the "precursor" v -radiation ϵV^R and explain the mechanism of interaction. It is convenient to transform equations into moving frame in this section.

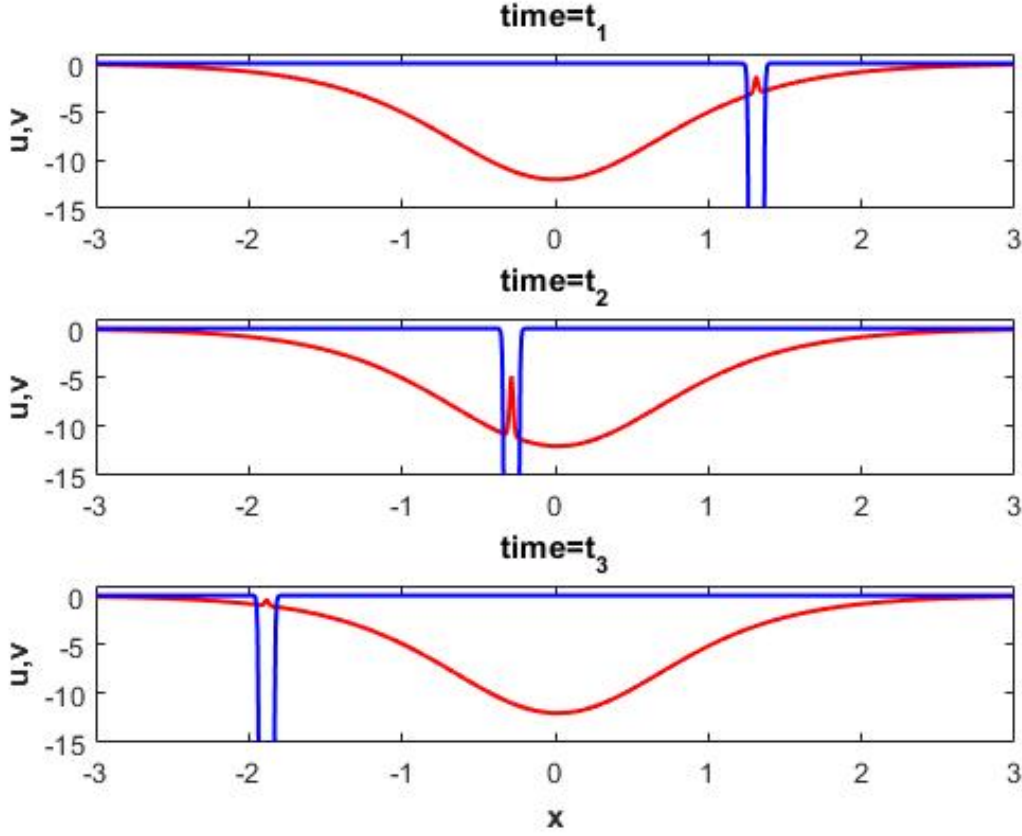


Figure 1. Observation of $U^F(x, X, T)$, a fleeting solitary structure inside $u(x, X, T)$. Slow and red one is u wave while the fast, sharp and blue one is v wave.

1.4. Numerical simulation with $\epsilon = 10^{-2}$

As for ansatz (5), $V^0(X, T) = K(X - cT)$ is approximately the original sharp soliton of wave v ; correspondingly, U^0 is the base of wave u , approximately $U^0 = K(x)$ since

$$K(x - c\epsilon^3 T) = K(x) - c\epsilon^3 K_x(x)T = K(x) + O(\epsilon^3).$$

At first glimpse, fleeting solitary structure

$$U^F(x, X, T) = u(x, X, T) - U^0(x) + o(\epsilon^0) = u(x, X, T) - K(x) + o(\epsilon^0) \quad (7)$$

is very eye-catching in figure 1; after a zoom-in, slow-moving "precursor" radiation ϵV^R (figure 2,6) is a more intriguing feature. Although less eye-catching, observations of U^F (figure 3) is naturally presented later on. Afterwards, U^B (figure 4) is more obscure (overshadowed by U^0) but validate our multiple scale model while establishing our model. Lastly, observations of V^F is difficult and actually do not play a major role while establishing our model but help us validate our model.

Under this philosophy, we next orderly present observation of U^F, V^R, U^B in this section (section 1.4).

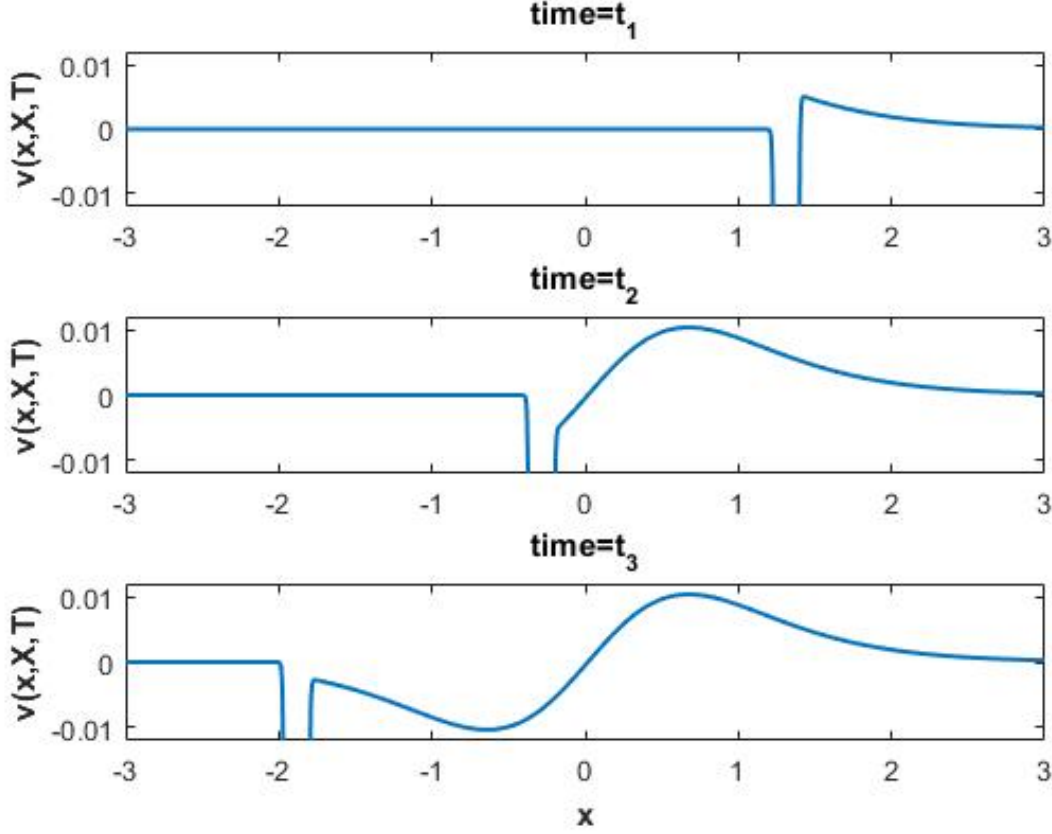


Figure 2. Observation of $\epsilon V^R(x, X, T)$ as precursor v radiation; observed from $v(x, X, T)$. Comparatively, figure 6 is a zoom-in in order to observe $V^R(x, X, T)$.

1.4.1. *Observation of U^F* Fleeting solitary structure U^F in figure 1 is very eye-catching; it is numerically evaluated by (7) and is plotted in figure 3.

From the simulation,

- (i) $\max_{x, X, T \in \mathbb{R}} U^F \simeq 6.57 \sim 6.87$, for $\epsilon = 10^{-2}, 1.4 \times 10^{-2}, 2 \times 10^{-2}, 2.5 \times 10^{-2}$. In other words, U^F appears to be a fleeting solitary structure in figure 3 such that $\max_{x, X, T \in \mathbb{R}} U^F(x, X, T)$ has nothing to do with ϵ .
- (ii) As time T goes, height of U^F seems proportional to $U^0 = K(x) + O(\epsilon^3)$. We prefer saying $U^F \propto \text{sech}^2(x)$ instead since $U^0 < 0$ and $\max |U^0| = 12$. Such preference (together with normalization of $R(x)$ later on) is very reader friendly since it , to some extent, ensures data consistency
 - in figure 2,6,7; table 2, representing size of U^B ;
 - in figure 4,8; first part of figure 10; table 1; derivation in (C.1), representing size of V^R .

This feature inspires us to plot $U^F(x, X, T)/\text{sech}^2(x)$ in figure 5. Notice the dominant part of $U^F(x, X, T)/\text{sech}^2(x)$ in figure 5 seems to be a stable fast-moving solitary structure $S^U(X - cT)$, we introduce $S^U(X - cT)$.

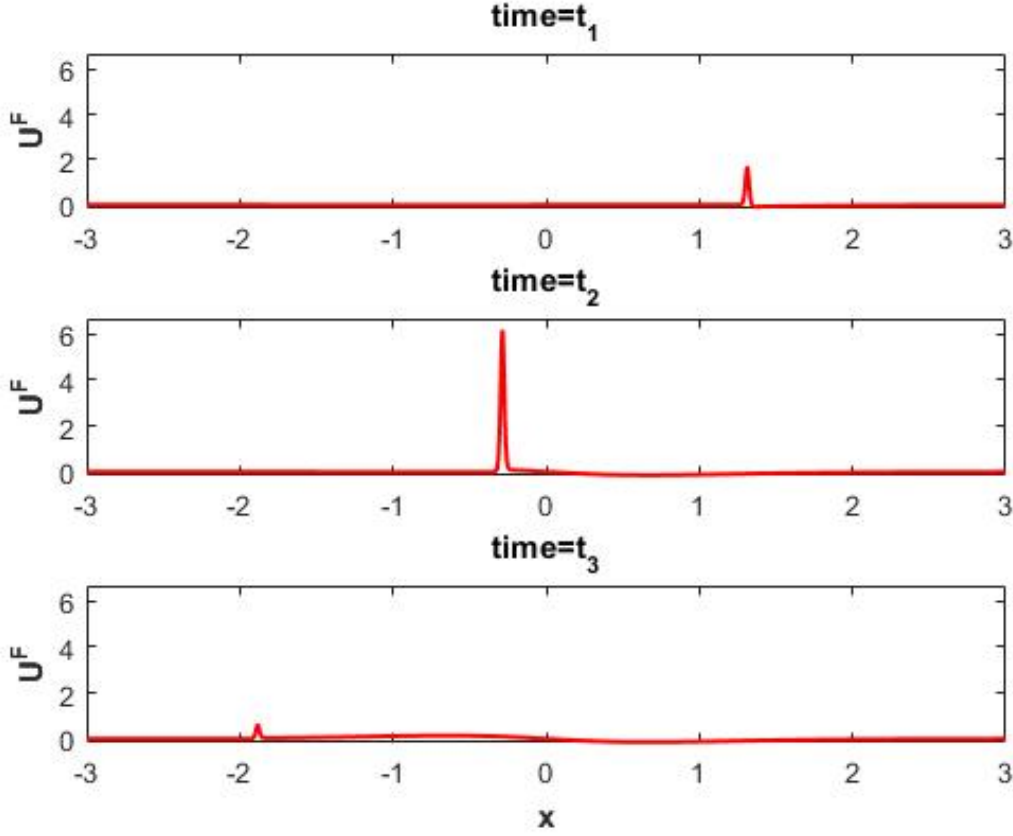


Figure 3. Snapshots of $U^F(x, X, T)$ in simulation with $\epsilon = 10^{-2}$. See Appendix A for details of data processing.

To conclude, we suppose that $U^F(x, X, T)$ has an exact solution in the form:

$$U^F(x, X, T) = \text{sech}^2(x) S^U(X - cT).$$

1.4.2. Observation of ϵV^R As one of goals of the paper, "precursor" radiation [18] in v is actually term $\epsilon V^R(x, X, T)$ at the bottom of $v(x, X, T)$. Figure 6 is a close-up of v near $x = 0$ and implies that "precursor" radiation is of order $O(\epsilon^1)$ and V^R looks like multiplication of

- (i) a fast-moving Heaviside-like structure $H^V(X - cT)$ with $\lim_{\xi \rightarrow -\infty} H^{\text{fast}}(\xi) = 0$ and $\lim_{\xi \rightarrow \infty} H^{\text{fast}}(\xi) = \max_{x, X} V^R(x, X, \infty)$ where $V^R(x, X, \infty) = \lim_{T \rightarrow \infty} V^R(x, X, T)$. It provides an effect that precursor v radiation seems scanned out by this fast Heaviside-like structure in figure 6.
- (ii) and a (normalized) centrosymmetric object $R(x) \propto K_x(x)$:

$$R(x) \doteq \frac{\sinh(x) \cosh^3(x)}{\max_x \sinh(x) \cosh^3(x)} = \frac{3\sqrt{3}}{2} \sinh(x) \cosh^3(x). \quad (8)$$

Notice we let $\max_x R(x) = -\min_x R(x) = 1$ so that C_V^R in (6) can represent height of V^R . Mentioned again, such normalization of $R(x)$ (together with preference

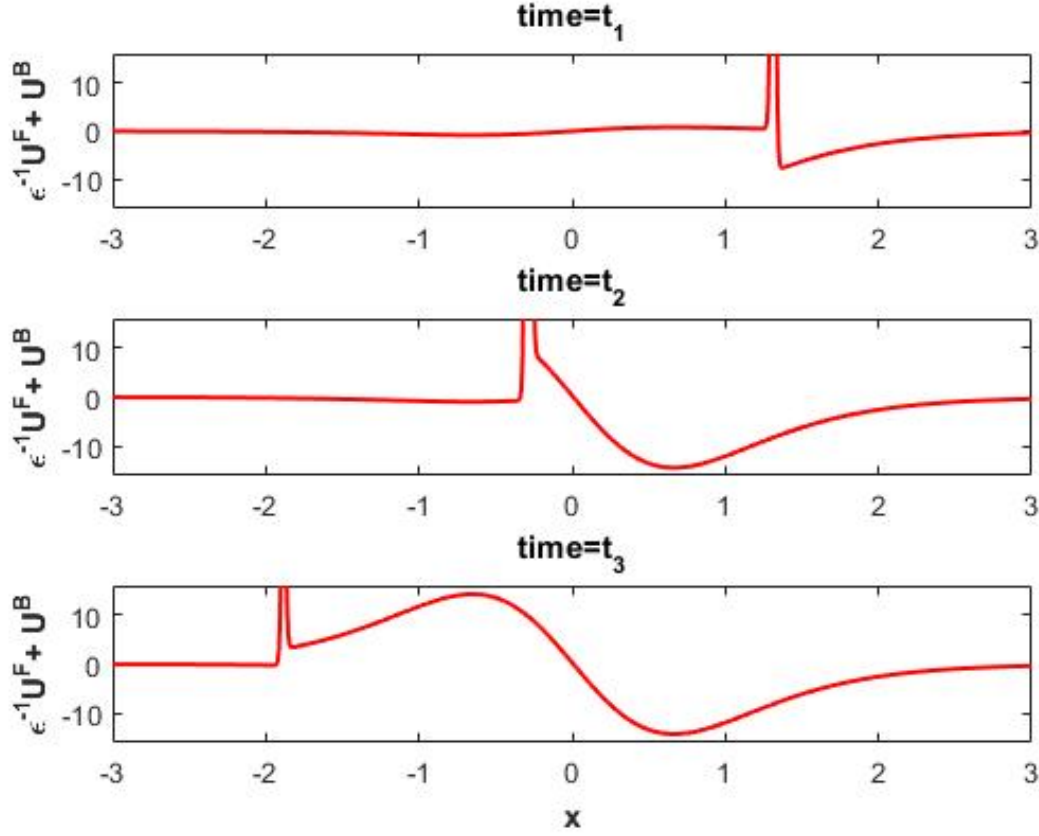


Figure 4. Observation of $R(x)$ shape and Heaviside like structure $H^U(X - cT)$ from $(\epsilon^{-1}U^F + U^B)(x, X, T)$ in simulation with $\epsilon = 10^{-2}$. See Appendix A for details of data processing.

of $\text{sech}^2(x)$ over $K(x)$) is reader friendly since it, to some extent, ensures data consistency

- in figure 2,6,7; table 2, representing size of U^B ;
- in figure 4,8; first part of figure 10; table 1; derivation in (C.1), representing size of V^R .

This feature inspires us to plot $V^R(x, X, T)/R(x)$ in figure 7 and we basically only expect it to be "Heaviside-like". Indeed, a Heaviside-like structure appears with $\lim_{\xi \rightarrow -\infty} H^V(\xi) = 0$ and $\lim_{\xi \rightarrow \infty} H^V(\xi) = \max_{x, X} V^R(x, X, \infty)$ (despite the (numerical) singularity of $\text{csch } x$, near the origin $x = 0$).

To conclude, we suppose that $V^R(x, X, T)$ has an exact solution in the form:

$$V^R(x, X, T) = R(x)H^V(X - cT).$$

1.4.3. Observation of ϵU^B After noticing that small bruise appear at the bottom of u in figure 3, a scrutiny reveals structure ϵU^B of order $O(\epsilon^1)$ and we zoom in figure 4: $U^B(x, X, T)$ looks like $R(x)$ in (8) multiplied by a Heaviside-like structure $H^U(X - cT)$.

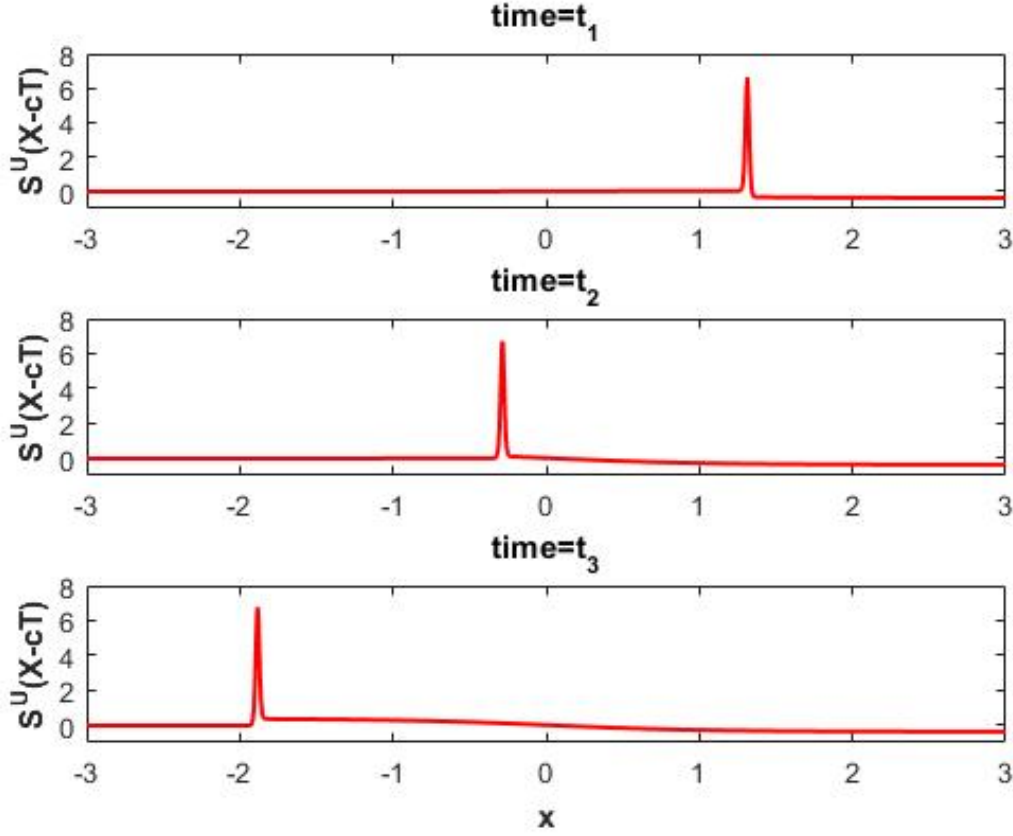


Figure 5. Observation of solitary $S^U(x, X, T)$ from snapshots of $U^F(x, X, T)/\text{sech}^2(x)$ in simulation with $\epsilon = 10^{-2}$. See Appendix A for details of data processing.

This feature inspires us to plot $U^B(x, X, T)/R(x)$ figure 8 and we basically only expect $H^U(X - cT)$ to be "Heaviside-like". Indeed, despite (numerical) singularity of $\text{csch } x$, near the origin $x = 0$ a Heaviside-like structure appears with $\lim_{\xi \rightarrow -\infty} H^U(\xi) = 0$ and $\lim_{\xi \rightarrow \infty} H^U(\xi) = \max_{x, X} U^B(x, X, \infty)$.

To conclude, we have shown that $U^B(x, X, T)$ has an exact solution in the form:

$$U^B(x, X, T) = R(x)H^U(X - cT).$$

2. Asymptotic approximation of the coupled KdV

We will first perform all of numerical simulations in the case with $\epsilon = 10^{-2}$. The essence of simulation is captured by this example, which can easily be generalized to the case with $\epsilon \rightarrow 0$.

These simulations also validate multiple-scale ansatz (5) and the fast-slow decomposition (10a, 10b, 10c, 10d) in case of $\epsilon \rightarrow 0$.

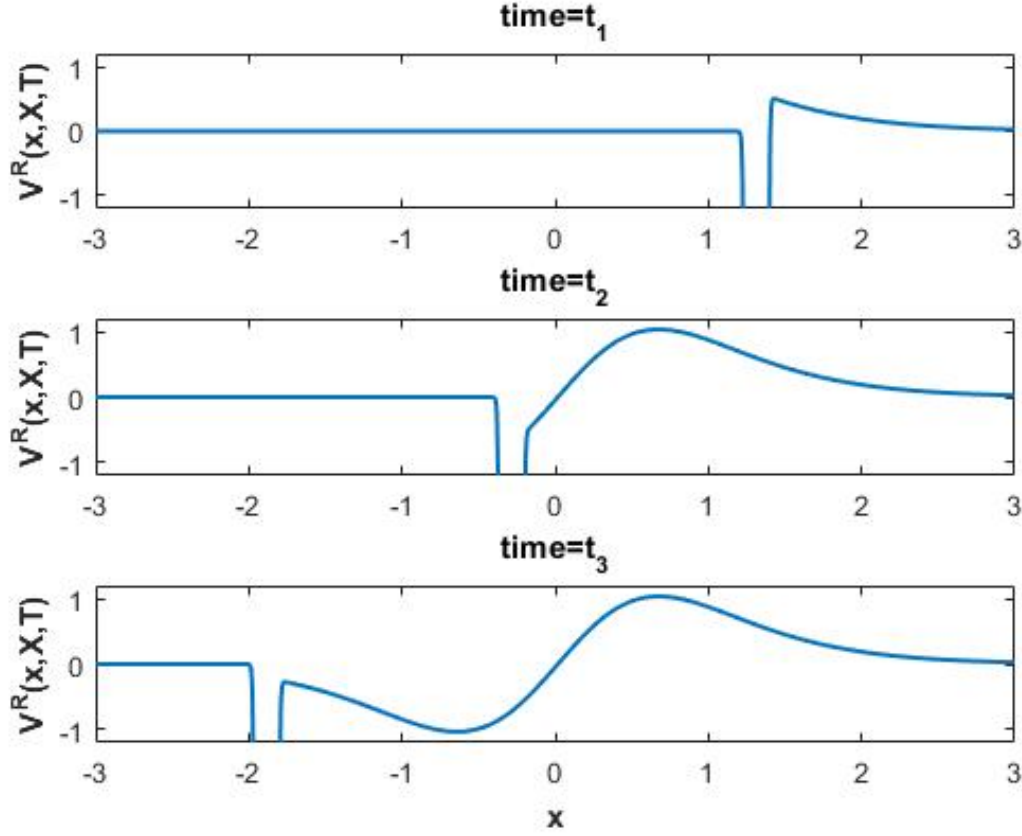


Figure 6. Observation of $R(x)$ shape and Heaviside like structure $H^U(X - cT)$ from $V^R(x, X, T)$ and observed directly at the bottom of $\epsilon^{-1}v(x, X, T)$. See Appendix A for details of data processing. A zoom-in of figure 2.

2.1. Multiple scale model: ansatz and equations

After concluding ansatz (5) from numerical simulations of (3), we substitute the ansatz (5) as well as $\frac{\partial}{\partial x} \rightarrow \epsilon^{-1} \frac{\partial}{\partial X} + \frac{\partial}{\partial x}$, $\frac{\partial}{\partial t} \rightarrow \epsilon^{-3} \frac{\partial}{\partial T}$ into Biello's equations (3) and get (3) with respect to different order of ϵ as:

$$\begin{aligned} & \epsilon^{-3} \mathcal{L}(U^F) + \epsilon^{-2} [\mathcal{L}(U^B) - 3U_{xXX}^F] \\ &= \frac{1}{2} \left\{ \epsilon^{-3} [(V^0 U^F)_X + U_0 V_{0,X}] + \epsilon^{-2} [(V^0 U^B)_X + (U_{0,x} + U_x^F) V^0] \right\}, \quad (9a) \end{aligned}$$

$$\begin{aligned} & \epsilon^{-5} \mathcal{K}(V^0) + \epsilon^{-3} [\mathcal{L}(V^F) + (V^0 V^F)_X] \\ &+ \epsilon^{-2} [\mathcal{L}(V^R) + V^0 V_x^F + (V^R V^0)_X - 3V_{xXX}^F] \\ &= \frac{1}{2} \left\{ \epsilon^{-3} [(V^0 U^F)_X + U_0 V_{0,X}] + \epsilon^{-2} [(V^0 U^B)_X + (U_{0,x} + U_x^F) V^0] \right\}. \quad (9b) \end{aligned}$$

where

$$\mathcal{L}(f) = f_T - f_{XXX}, \quad \mathcal{K}(f) = \mathcal{L}(f) + ff_X.$$

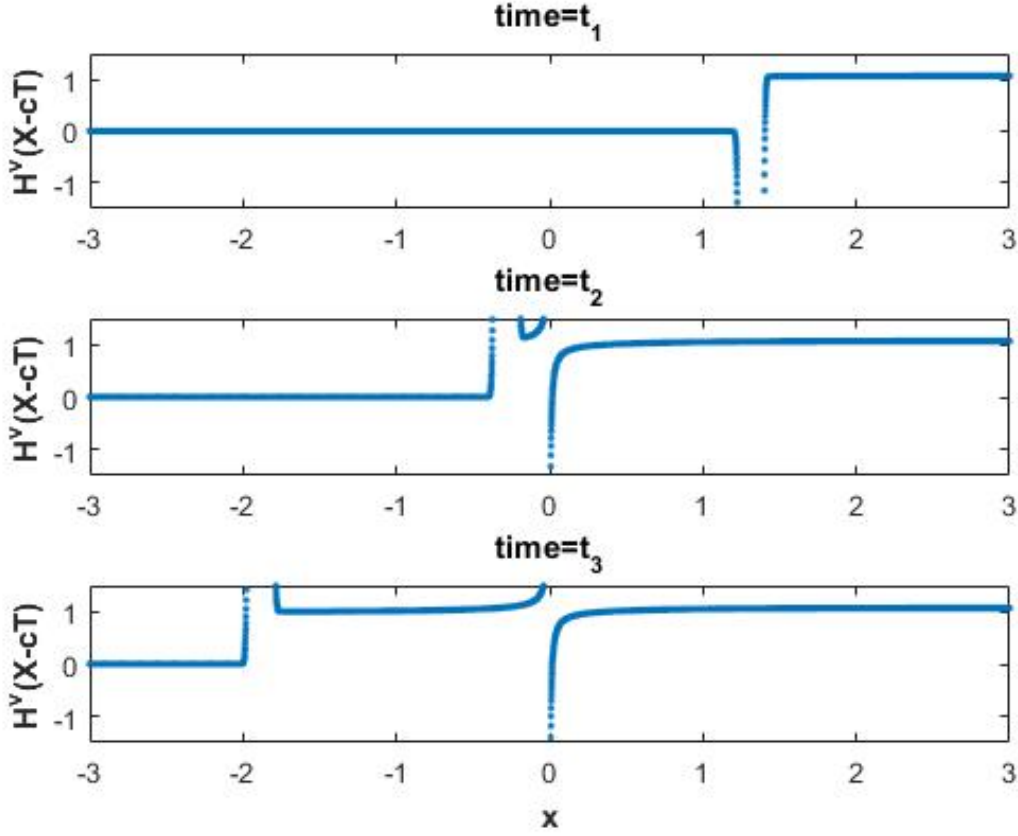


Figure 7. Heaviside-like structure $H^V(x - cT)$ from $V^R(x, X, T)/R(x)$ in simulation with $\epsilon = 10^{-2}$. See Appendix A for details of data processing.

From (9b), we can notice that U^F, V^F, U^B are indispensable for solving the equation for V^R although "precursor" radiation V^R is our focus of attention in the simulation.

2.2. Fast-slow decomposition

Fast-slow decomposition basically means we decompose functions with respect to two pairs of time-length scales – a small length scale X with fast time T , and a large length scale x . At first glimpse, fast-slow decomposition just seems to be an outcome of multiple scale analysis. However, the decomposition is particularly listed since

- (i) together with "Heaviside-like" structures H^U, H^V , it plays a crucial role to validate the ansatz;
- (ii) it plays an important role in reducing PDEs for U^F, V^F, U^B, V^R into ODEs (16, 18, 20, 22) in section 2.3.

Notice that in the stationary frame of reference, the V^0 soliton does not depend on τ . The equation (14a) for U^F comes endowed with boundary values $U^F(x, \xi, \tau) \rightarrow 0$ as $\xi \rightarrow \pm\infty$ and initial condition $U^F(x, \xi, T) \rightarrow 0$ as $\tau \rightarrow -\infty$.

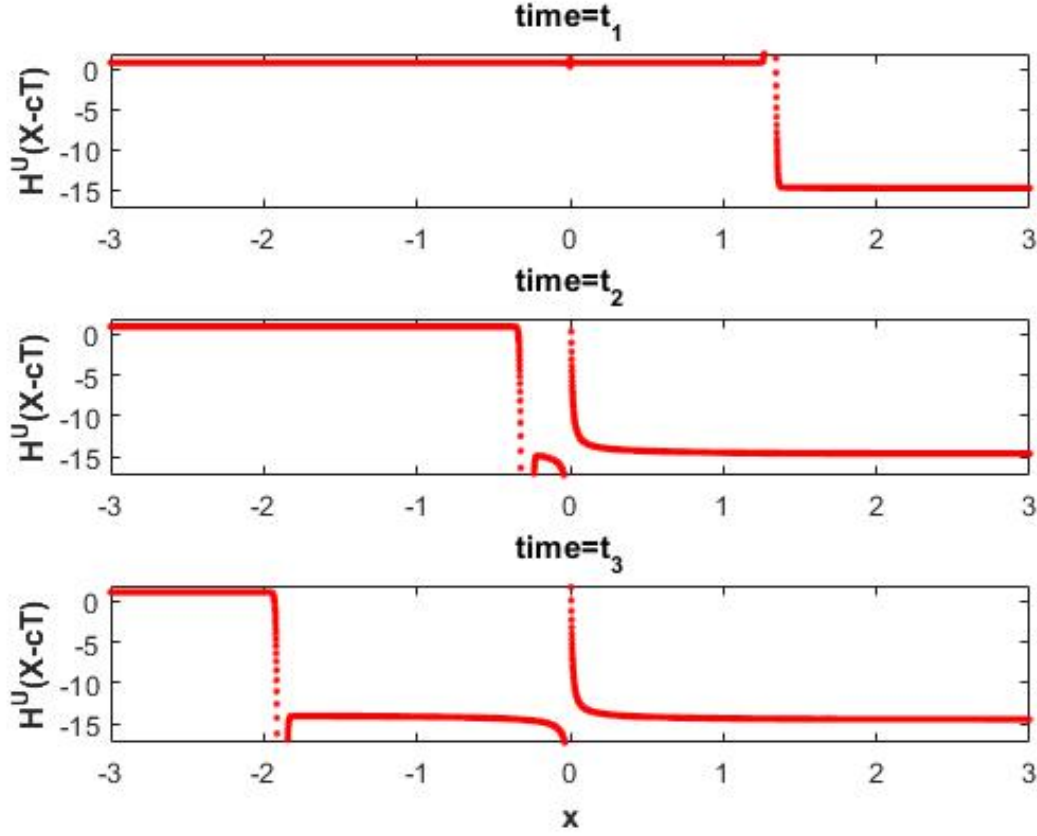


Figure 8. Heaviside-like structure $H^U(X - cT)$ from $U^B(x, X, T)/R(x)$ in the simulation with $\epsilon = 10^{-2}$. See Appendix A for details of data processing.

Eventually, the decomposition turn to be:

$$U^F(x, X, T) = \text{sech}^2(x)S^U(X - cT), \quad (10a)$$

$$V^F(x, X, T) = \text{sech}^2(x)S^V(X - cT), \quad (10b)$$

$$U^B(x, X, T) = R(x)H^U(X - cT), \quad (10c)$$

$$V^R(x, X, T) = R(x)H^V(X - cT). \quad (10d)$$

or for short:

$$\begin{aligned} U^F(x, \xi, \tau) &= \text{sech}^2(x)S^U(\xi), & V^F(x, \xi, \tau) &= \text{sech}^2(x)S^V(\xi), \\ U^B(x, \xi, \tau) &= R(x)H^U(\xi), & V^R(x, \xi, \tau) &= R(x)H^V(\xi), \end{aligned}$$

since U_0 component of wave u almost unmoved with respect to wave v . Here moving frame $\xi = X - cT$ is presented in advance and will be utilized as a customized frame while reducing PDEs into ODEs in section 2.3.

2.3. Solving for Biello's equation in moving frame

Substituting ansatz (5) into (3), Biello's equations become (9a, 9b), which can be written out versus different order of ϵ as:

$$\mathcal{L}(U^F) - \frac{[V^0 U^F]_X}{2} \equiv \frac{U_0 V_{0,X}}{2}, \quad (11a)$$

$$\mathcal{L}(V^F) + [V^0 V^F]_X \equiv \frac{[U^F V^0]_X + U_0 V_{0,X}}{2}, \quad (11b)$$

$$\mathcal{L}(U^B) - [V^0 U^B]_X \equiv [U_{0,x} + U_x^F] V^0 + 3U_{xXX}^F, \quad (11c)$$

$$\mathcal{L}(V^R) + [V^0 V^R]_X \equiv [V^0 U^B]_X + [U_{0,x} + U_x^F] V^0 - V^0 V_x^F + 3V_{xXX}^F. \quad (11d)$$

where

$$\mathcal{L}(f) = f_T - f_{XXX}, \quad U_0 = K(x), \quad V^0 = K(X - cT). \quad (12)$$

These equations have simple structures, three aspects of which are very illuminating:

- (i) They each have an in-homogeneity listed, separately, on right hand sides of each equation for U^F, V^F, U^B, V^R .
- (ii) The first order T -derivatives and the third order X -derivatives are endowed by linear KdV operator L .
- (iii) The in-homogeneous terms for V^F, U^B only involves U^F ; the one for V^R involves U^F, V^F . Therefore, we can solve equations V^F, U^B after solving U^F and eventually solve V^R .

2.3.1. Perspectives in moving frame In the limit that $\epsilon \rightarrow 0$, it is tantamount to viewing equations in moving frame $\xi(X, T) \equiv X - cT$, $\tau(X, T) \equiv T$ which is naturally inspired by numerical simulations by referring to figure 3, 4, 6 for U^F, U^B, V^R and correspondingly, figure 5, 8, 7 for S^U, H^U, H^V . Chain rule implies

$$\begin{aligned} \left[\frac{\partial}{\partial X}, \frac{\partial}{\partial T} \right] &\equiv \left[\frac{\partial}{\partial \xi}, \frac{\partial}{\partial \tau} \right] \begin{bmatrix} \frac{\partial \xi}{\partial X}(X, T) & \frac{\partial \xi}{\partial T}(X, T) \\ \frac{\partial \tau}{\partial X}(X, T) & \frac{\partial \tau}{\partial T}(X, T) \end{bmatrix} \equiv \left[\frac{\partial}{\partial \xi}, \frac{\partial}{\partial \tau} \right] \begin{bmatrix} 1 & 4 \\ 0 & 1 \end{bmatrix} \\ \Leftrightarrow \quad \frac{\partial}{\partial X} &\equiv \frac{\partial}{\partial \tau} - c \frac{\partial}{\partial \xi}, \quad \frac{\partial}{\partial T} \equiv \frac{\partial}{\partial \tau}, \end{aligned}$$

or for short,

$$\begin{aligned} \xi(X, T) &\equiv X - cT, \quad \tau(X, T) \equiv T \\ \Rightarrow \frac{\partial}{\partial X} &\equiv \frac{\partial}{\partial \tau} - c \frac{\partial}{\partial \xi}, \quad \frac{\partial}{\partial T} \equiv \frac{\partial}{\partial \tau}. \end{aligned} \quad (13)$$

Performing the changing of variables on equations (11a, 11b, 11c, 11d) and substituting $U_0 \equiv K(x), V^0 \equiv K(\xi)$ by (12) incidentally. We find (11a) for U^F is a linear, in-homogeneous PDE independent of V^F, U^B, V^R ,

$$\mathcal{L}(U^F) - \frac{[K(\xi)U^F]_\xi}{2} \equiv \frac{K(x)K(\xi)_\xi}{2}, \quad (14a)$$

where linear KdV operator turns into $\mathcal{L}(f) \equiv f_\tau - cf_\xi - f_{\xi\xi\xi}$. by chain rule (13).

(11b,11c) for V^F, U^B are also linear, each with an in-homogeneity which depends on U^F ,

$$\mathcal{L}(V^F) + [K(\xi)V^F]_\xi \equiv \frac{K(x)U_\xi^F + K(x)K(\xi)_\xi}{2}, \quad (14b)$$

$$\mathcal{L}(U^B) - [K(\xi)U^B]_\xi \equiv [F_x(x) + U_x^F] K(\xi) + 3U_{x\xi\xi}^F. \quad (14c)$$

Finally, (11d) for V^R is also linear, with an in-homogeneity which depends on U^F, V^F, U^B ,

$$\begin{aligned} & \mathcal{L}(V^R) + [K(\xi)V^R]_\xi \\ & \equiv [K(\xi)U^B]_\xi + [F_x(x) + U_x^F] K(\xi) - K(\xi)V_x^F + 3V_{x\xi\xi}^F. \end{aligned} \quad (14d)$$

Under this philosophy, in order to predict V^R , we need to first orderly predict U^F, V^F, U^B . Later in this section (section 2.3), we will predict them in order of U^F, V^F, U^B, V^R .

2.3.2. Solution of U^F From fast-slow decomposition, we know that (14a) has an exact solution in the form:

$$U^F(x, \xi, \tau) = \text{sech}^2(x)S^U(\xi), \quad (15)$$

where we actually seek the solution for U^F independent of τ .

Substituting (15) into (14a) we find the ODE for G :

$$S_{\xi\xi}^U - [4 + 6 \text{sech}^2(\xi)] S^U = -72 \text{sech}^2(\xi). \quad (16)$$

2.3.3. Solution of V^F Again according to fast-slow decomposition, we seek a solution of the form:

$$V^F(x, \xi, \tau) = \text{sech}^2(x)S^V(\xi), \quad (17)$$

After substituting (15, 17) into equation (14b), we find the ODE for $S^V(\xi)$

$$S_{\xi\xi}^V - [4 - 12 \text{sech}^2(\xi)] S^V = 6[S^U(\xi) - 12] \text{sech}^2(\xi). \quad (18)$$

with boundary values $\lim_{\xi \rightarrow -\infty} S^V(\xi) = \lim_{\xi \rightarrow \infty} S^V(\xi) = 0$ according to figure 5 of numerical simulation. Figure D1 (second) plots S^V with $S^V(-10) = S^V(10) = 0$.

2.3.4. Solution of U^B Again according to fast-slow decomposition, we seek a solution of the form:

$$U^B(x, \xi, \tau) = R(x)H^U(\xi). \quad (19)$$

After substituting (15, 17, 19) into equation (14c), we find that the ODE for $H^U(\xi)$

$$H_{\xi\xi}^U - [4 + 6 \text{sech}^2(\xi)] H^U = \frac{4\sqrt{3}}{3} \left[2 \int_{-\infty}^{\xi} [12 - S^U(\eta)] \text{sech}^2(\eta) d\eta + S_\xi^U \right]. \quad (20)$$

with left boundary value $\lim_{\xi \rightarrow -\infty} H^U(\xi) = 0$ according to figure 8 from numerical simulation; by taking $\lim_{\xi \rightarrow \infty}$ on both sides of (20), right boundary value of appears as $H^U(10) = -\frac{4\sqrt{3}}{9} \int_{\mathbb{R}} S^U(\eta) d\eta = -15.37$ (see Appendix C for detail). To conclude, figure 10 (first) shows Heaviside-like H^U .

2.3.5. Solution of V^R Finally, we seek a solution of the form for "precursor" radiation V^R :

$$V^R(x, \xi, \tau) = R(x)H^V(\xi). \quad (21)$$

After substituting (15, 17, 19, 21) into equation (14d), we find that the terms give an equation for $H^V(\xi)$

$$H_{\xi\xi}^V - [4 - 12 \operatorname{sech}^2(\xi)]H^V = \frac{4\sqrt{3}}{3} \cdot \left[H^U(\xi) \operatorname{sech}^2(\xi) + S_{\xi}^V + 2 \int_{-\infty}^{\xi} [12 - S^U(\eta) + 2S^V(\eta)] \operatorname{sech}^2(\eta) d\eta \right]. \quad (22)$$

with left boundary value $\lim_{\xi \rightarrow -\infty} H^V(\xi) = 0$ according to figure 7 from numerical simulation; by taking $\lim_{\xi \rightarrow \infty}$ on both sides of (22), right boundary value appears as $H^V(10) = -\frac{4\sqrt{3}}{9} \int_{\mathbb{R}} S^V(\eta) d\eta \simeq 4.11$ (see Appendix C for detail). To conclude, figure 10 (second) shows Heaviside-like H^V .

2.4. Conclusion of solutions

With our multiple-scale model, we can predict U^F, V^F, U^B, V^R in ansatz (5). Details of analytic solution utilizes fast-slow decomposition (10a, 10b, 10c, 10d) and solve fast-moving part of them via ODEs for S^U, S^V, H^U, H^V .

As a special case, ϵV^R , the **energy exchange** and this subtle **"precursor" radiation** can be analytically predicted. Our multiple scale model predicts (6):

$$\epsilon V^R = \epsilon C_V^R R(x),$$

as $T \rightarrow \infty$ where $C_V^R = \lim_{\xi \rightarrow \infty} H^V(\xi) = 4.11$.

Comparisons between model predictions and numerical simulation (with various ϵ) are summarized in section 3.

3. Comparison to Numerical Simulations

We compare our model predictions to numerical simulations of the Biello's equation (3). The system is solved in a doubly periodic domain using a pseudo-spectral method. These simulations were performed with $\Delta x = \frac{25}{N}$ for $N = 2^{15}$, with $\epsilon = 0.1, 0.025, 0.02, 0.014, 0.01$, where $\frac{\Delta t}{(\Delta x)^3} \simeq 1$. All solutions were monitored for conservation of energy, Hamiltonian and (two) mean fields to a relative accuracy of at least 10^{10} . The last nonlinear energy-conserved term is also an important feature in

Table 1. Maximum of U^F and second local extrema of U^B : between model predictions and numerical simulations (BI : data before interaction; DI : data during interaction).

- numerical simulations: when it comes to $\max U^F$, we are evaluating maximum of solitary structure shown in figure 3;
speaking of second local extrema of U^B , we refer to the local minima on the right of figure 4;
- Predicted values: when it comes to predicted $\max U^F$, predicted U^F is from fast-slow decomposition (15) where S^U from (16) is numerically presented via finite difference method with boundary values $\lim_{\xi \rightarrow \pm\infty} S^U(\xi) = 0$ (see figure 9 for consistency of S^U);
speaking of second local extrema of U^B , we refer to the local minima of U^B from fast slow decomposition (19). H^U from (20) is numerically presented via finite difference method with boundary values $H^U(-10) = 0, H^U(10) = -\frac{4\sqrt{3}}{9} \int_{\mathbb{R}} S^U(\eta) d\eta \simeq -15.37$ (see figure 10).

ϵ	$\max U^F$	second local extrema of U^B
prediction	6.68	-15.37
0.1	6.66 \sim 6.87	
0.0025	6.57 \sim 6.67 BI	-16.02 \sim -16.06
0.002	6.69 \sim 6.71	-15.90 \sim -15.91
0.0014	6.69 \sim 6.70	-15.23 \sim -15.80
0.001	6.62 \sim 6.70	-15.31 \sim -15.66

wave turbulence [25]. Interestingly [26] points out our Biello-Majda system has only these four conserved quantities.

In table 1, we show comparison of $\max U^F$ and second local extrema of U^B between predicted values numerical simulations. We see excellent agreement for U^F, U^B between the model predictions and the numerical solutions.

3.1. Comparison of S^U, H^U, H^V

It is not just maximum of U^F , minimum of V^F , second local extrema of U^B, V^R where we see good agreement between theory and simulation.

Due to fast-slow decomposition, instead of comparing U^F, V^F, U^B, V^R , we compare solitary S^U, S^V , Heaviside-like H^U, H^V for the sake of convenience. This is not only because S^U, S^V, H^U, H^V can be viewed in moving frame $\xi = X - cT$, but S^U, S^V, H^U, H^V have much simpler structures as well - solitary S^U, S^V and Heaviside-like H^U, H^V .

Figure 9 shows S^U

- predicted by asymptotic model from (16) numerically via finite difference method with boundary condition $\lim_{\xi \rightarrow \pm\infty} S^U = 0$ and
- the ones from simulations plotted via $U^F(x, X, T)/\text{sech}^2(x)$ in section 1.4.1 (same philosophy as figure 5).

Table 2. Maximum of V^F and second local extrema of V^R : model prediction and numerical simulations (BI : data before interaction; DI : data during interaction).

- numerical simulations: when it comes to $\max V^F$, we are evaluating minimum of solitary structure shown in section Appendix D where $\min V^F = \min S^V$ due to fast-slow decomposition (17);
speaking of second local extrema of V^R , we refer to the local maxima on the right of figure 6;
- Predicted values: when it comes to predicted $\max V^F$, predicted V^F is from fast-slow decomposition (17) where S^V from (18) is numerically presented via finite difference method with boundary values $\lim_{\xi \rightarrow \pm\infty} S^V(\xi) = 0$ (see figure D1);
speaking of second local extrema of U^B , we refer to the local maxima of V^R from fast slow decomposition (21). H^V from (22) is numerically presented via finite difference method with boundary values $H^V(-10) = 0, H^V(10) = -\frac{4\sqrt{3}}{9} \int_{\mathbb{R}} S^V(\eta) d\eta = -4.11$ (see figure 10).

ϵ	$\min V^F$	second local extrema of V^R
prediction	-9.77	4.11
0.75	-6.57^{DI}	hard to detect
0.1	$-7.20 \sim -7.09^{BI}$ $-6.83 \sim -6.28^{DI}$	$1.11 \sim 1.13$
0.0025	$-6.06 \sim -6.00^{BI}$ $-5.90 \sim -5.86^{DI}$	$1.12 \sim 1.14$
0.002	$-5.90 \sim -6.02$	$1.11 \sim 1.13$
0.0014	$-5.91 \sim -5.90^{BI}$ $-5.77 \sim -5.75^{DI}$	$1.01 \sim 1.10$
0.001	$-5.89 \sim -5.86^{BI}$ $-5.88 \sim -5.86^{BI2}$ $-5.76 \sim -5.74^{DI}$	$1.04 \sim 1.10$

The solitary structure is evident and our asymptotic model precisely predict solitary U^F since two plots overlap each other.

Figure 10 (first) shows Heaviside-like H^U predicted by asymptotic model from (20) numerically via finite difference method with boundary condition $\lim_{\xi \rightarrow -\infty} H^U = 0$ and $\lim_{\xi \rightarrow -\infty} H^U = -15.37$. This is in excellent agreement with simulation result in figure 4,8 and therefore predict the exact size of U^B .

Finally, figure 10 (right) shows Heaviside-like H^V predicted by asymptotic model from (22) numerically via finite difference method with boundary condition $\lim_{\xi \rightarrow -\infty} H^V = 0$ and $\lim_{\xi \rightarrow \infty} H^V \simeq 4.11$. Although this differs from asymptotic simulation shown in figure 2,6,7, it is in agreement with the sign and relative size of V^R, H^V . Table 2 concludes the difference.

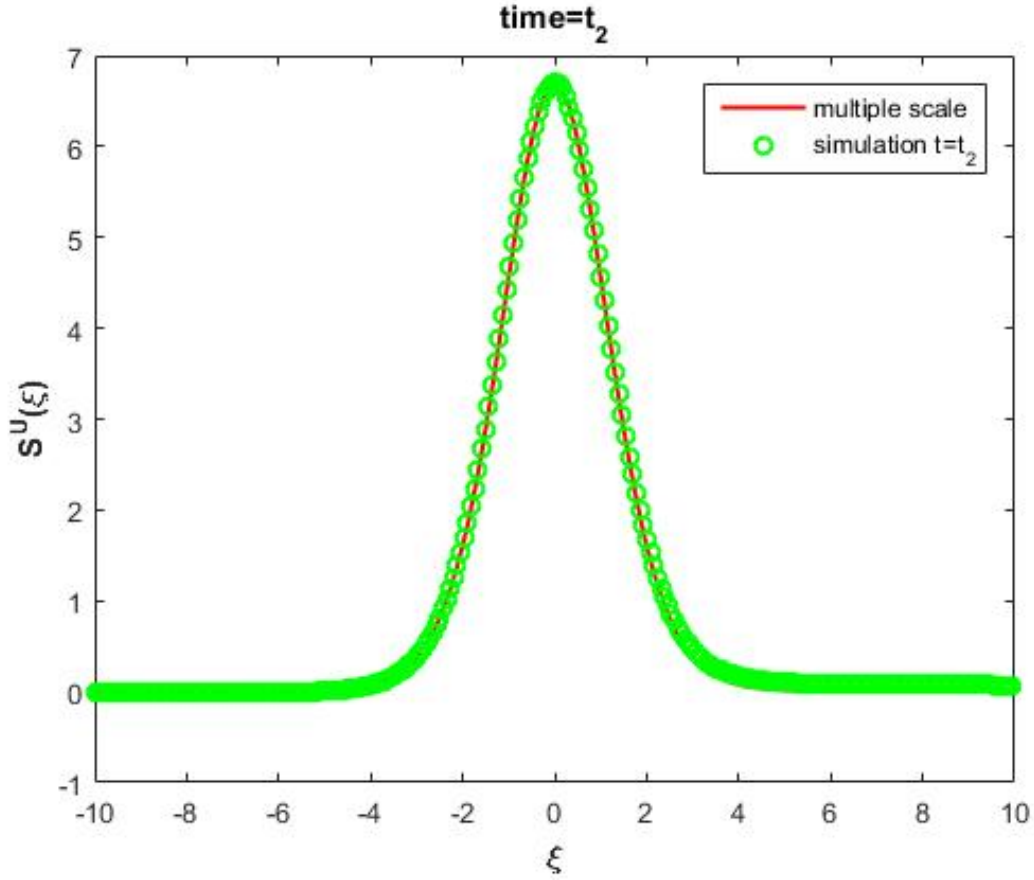


Figure 9. $S^U(\xi)$ predicted by asymptotic model from ODE (16) coincides with ones from numerical simulation:

the predicted $S^U(\xi)$ is plotted via finite difference method with Cauchy boundary condition $S^U(-10) = S^U(10) = 0$.

$S^U(\xi)$ from numerical simulation is plotted via $U^F(x, X, T)/\text{sech}^2(x)$. See Appendix A for details of data processing.

3.2. Observation and verification of V^F, S^V

Numerical observation of V^F is quite difficult once realizing $\epsilon^{-2}V^0$ part of wave v is very sharp. On the other hand, we can validate our model by validating corresponding fast-slow decomposition (10b).

However, exact sizes of V^F, S^V are inconsistent between the model prediction and simulations. According to (C.2), it is precisely integral of S^V that determines right boundary value for H^V , which is the important feature for H^V .

Details of this solitary structure S^V (figure D1) with two small bumps at two sides is shown in app:observation of H.

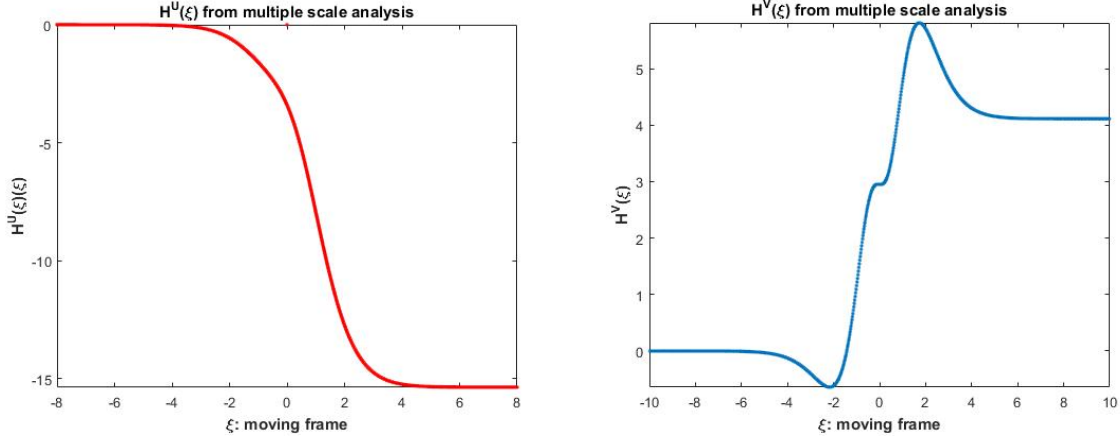


Figure 10. First: $H^U(\xi)$ predicted by asymptotic model from (20) and numerically plotted via finite difference method with Cauchy boundary condition $H^U(-10) = 0$, $H^U(10) = -\frac{4\sqrt{3}}{9} \int_{\mathbb{R}} S^U(\eta) d\eta \simeq -15.37$; second: $H^V(\xi)$, predicted by asymptotic model from (22) and numerically plotted via finite difference method with Cauchy boundary condition $H^V(-10) = 0$, $H^V(10) = -\frac{4\sqrt{3}}{9} \int_{\mathbb{R}} S^V(\eta) d\eta \simeq 4.11$.

4. Conclusion

4.1. Theoretical contribution

Our multiple scale model

- (i) predict mechanism of interaction within this nonlinearly coupled KdV equations:
precursor v -radiation is formed firstly; then it interacts with u , forming u -radiation and v -radiation in-situ.
- (ii) predict with an analytic, asymptotic approximation, the "precursor" radiation generated during interaction of solitary waves in Biello's system.

Our establishment of model, motivated by actual numerical simulations, can be applied to different situations, with different models.

4.2. Back to atmospheric background

This solution also gives an essential theoretical piece of the physical explanation for the behavior of radiation in Biello's system that may lead to a deeper understanding of solitary interaction within the system.

In atmosphere-ocean community, our work can be thought as asymptotic analysis of the nonlinear traveling waves [19, 27, 28] as soliton-like solutions leave behind small scale features after interaction. Furthermore, implications of these structures and interactions for atmospheric tropical/midlatitude behavior is necessary [18]. This sort of nonlinear interaction involving equatorial baroclinic and barotropic Rossby modes might be related to diurnal variations of deep convection in the tropics [21].

Back to atmospheric background, our work can be treated as asymptotic analysis of the nonlinear traveling waves [19, 27, 28] as soliton-like solutions leave behind small

scale features. Furthermore, much more work is necessary in order to understand the implications of interactions for atmospheric tropical/midlatitude connections [18]. This sort of nonlinear interaction involving equatorial baroclinic and barotropic Rossby modes might be directly related to diurnal variations of deep convection in the tropics [21].

5. Acknowledgments

Thanks for Trevor Halsted's early numerical experiments showing radiation after interaction. The first author thanks Prof. Biello for two-year patient guidance as well as his parents and Nanjing University (undergraduate institution) for financial and official/legitimate support on five-month exchange opportunity to UC Davis in 2014.

Appendix A. Processing of simulation data to plot figures

As for

- figure 3, we plot $u(x, X, T) - K(x)$ due to (7);
- figure 4, $\epsilon^{-1} (U^F + \epsilon U^B)(x, X, T) = \epsilon^{-1} (u(x, X, T) \cosh^2(x) + 12) + o(\epsilon^0)$ in simulation with $\epsilon = 10^{-2}$.
- figure 5 and part of figure 9, $\frac{U^F(x, X, T)}{\text{sech}^2(x)}$ are attained from simulation via

$$\begin{aligned} & \frac{U^F(x, X, T)}{\text{sech}^2(x)} \\ &= \frac{u(x, X, T) - (K(x) + o(\epsilon^0))}{\text{sech}^2(x)} = \frac{u(x, X, T) + 12 \text{sech}^2(x)}{\text{sech}^2(x)} + o(\epsilon^0) \\ &= \cosh^2(x) u(x, X, T) + 12 + o(\epsilon^0). \end{aligned}$$

- figure 7, $\frac{V^R(x, X, T)}{R(x)}$ are attained from simulation data by

$$\begin{aligned} & \frac{V^R(x, X, T)}{R(x)} = \epsilon^{-1} \frac{\epsilon V^R(x, X, T)}{R(x)} \\ &= \frac{\epsilon^{-1}}{R(x)} \{v(x, X, T) - [\epsilon^{-2} V^0(X, T) + V^F(x, X, T) + o(\epsilon^0)]\} \\ &= \frac{\epsilon^{-1}}{R(x)} \{v(x, X, T) - [\epsilon^{-2} V^0(X, T) + V^F(x, X, T)]\} + o(\epsilon^0) \\ &\simeq \frac{\epsilon^{-1} v(x, X, T)}{R(x)}. \end{aligned}$$

Above approximation is admissible just because $\epsilon^{-2} V^0(X, T) + V^F(x, X, T)$ are narrow enough not to affect our observations;

- figure 8, $\frac{U^B(x, X, T)}{R(x)}$ is attained from simulation via

$$\frac{U^B(x, X, T)}{R(x)} = \frac{\epsilon^{-1}}{R(x)} \cdot \epsilon U^B(x, X, T)$$

$$\begin{aligned}
&= \frac{\epsilon^{-1}}{R(x)} \cdot \{u(x, X, T) - [K(x) + U^F(x, X, T) + o(\epsilon^1)]\} \\
&= \frac{\epsilon^{-1}}{R(x)} \{u(x, X, T) - [K(x) + U^F(x, X, T)]\} + o(\epsilon^0) \\
&\simeq \frac{\epsilon^{-1} [u(x, X, T) - K(x)]}{R(x)} + o(\epsilon^0).
\end{aligned}$$

Above approximation is admissible since U^F is narrow enough not to affect our observations;

- figure 10, part of figure 9 and second part of figure D1, are plotted from data via finite difference method solving Cauchy boundary value problems with two boundary values assigned at $\xi = -10, \xi = 10$. 20,000 points are considered.

Appendix B. Derivation of WKB equations in section 2.1

Since

$$\begin{aligned}
&u_t - u_{xxx} + uu_x \text{ (use (5))} \\
&= \epsilon^{-3} U_T^F + \epsilon^{-2} U_T^B - [\epsilon^{-3} U_{XXX}^F + 3\epsilon^{-2} U_{xXX}^F + \epsilon^{-2} U_{XXx}^B] + o(\epsilon^{-2}) \\
&= \epsilon^{-3} \mathcal{L}(U^F) + \epsilon^{-2} [\mathcal{L}(U^B) - 3U_{xXX}^F] + o(\epsilon^{-2}),
\end{aligned}$$

$$\begin{aligned}
&v_t - v_{xxx} + vv_x \\
&= (\text{ use (5) }) \epsilon^{-5} V_T^0 + \epsilon^{-3} V_T^F + \epsilon^{-2} V_T^R \\
&\quad - [\epsilon^{-5} V_{XXX}^0 + \epsilon^{-3} V_{XXX}^F + 3\epsilon^{-2} V_{xXX}^F + \epsilon^{-2} V_{XXx}^R] \\
&\quad + [\epsilon^{-2} V^0 + V^F + \epsilon V^R] [\epsilon^{-3} V_{0,X} + \epsilon^{-1} V_X^F + (V_x^F + V_X^R)] + o(\epsilon^{-2}) \\
&= \epsilon^{-5} V_T^0 + \epsilon^{-3} V_T^F + \epsilon^{-2} V_T^R \\
&\quad - [\epsilon^{-5} V_{XXX}^0 + \epsilon^{-3} V_{XXX}^F + 3\epsilon^{-2} V_{xXX}^F + \epsilon^{-2} V_{XXx}^R] \\
&\quad + \epsilon^{-5} V^0 V_X^0 + \epsilon^{-3} (V^F V_{0,X} + V^0 V_X^F) \\
&\quad + \epsilon^{-2} [V^0 (V_x^F + V_X^R) + V_{0,X} V^R] + o(\epsilon^{-2}) \\
&= \epsilon^{-5} \mathcal{K}(V^0) + \epsilon^{-3} [\mathcal{L}(V^F) + (V^0 V^F)_X] \\
&\quad + \epsilon^{-2} [\mathcal{L}(V^R) - 3V_{xXX}^F + V^0 V_x^F + (V^0 V^R)_X] + o(\epsilon^{-2}),
\end{aligned}$$

and

$$\begin{aligned}
&(uv)_x \\
&= (\text{ use (5) }) [U^0 + U^F + \epsilon U^B] \epsilon^{-3} V_X^0 \\
&\quad + [\epsilon^{-1} U_X^F + U_x^0 + U_X^B] \epsilon^{-2} V^0 + o(\epsilon^{-2}) \\
&= \epsilon^{-3} [U^0 V_X^0 + (U^F V^0)_X] \\
&\quad + \epsilon^{-2} [(U^B V^0)_X + (U_x^0 + U_x^F) V^0] + o(\epsilon^{-2}),
\end{aligned}$$

where

$$\mathcal{L}(f) = f_T - f_{XXX}, \quad \mathcal{K}(f) = \mathcal{L}(f) + f f_X,$$

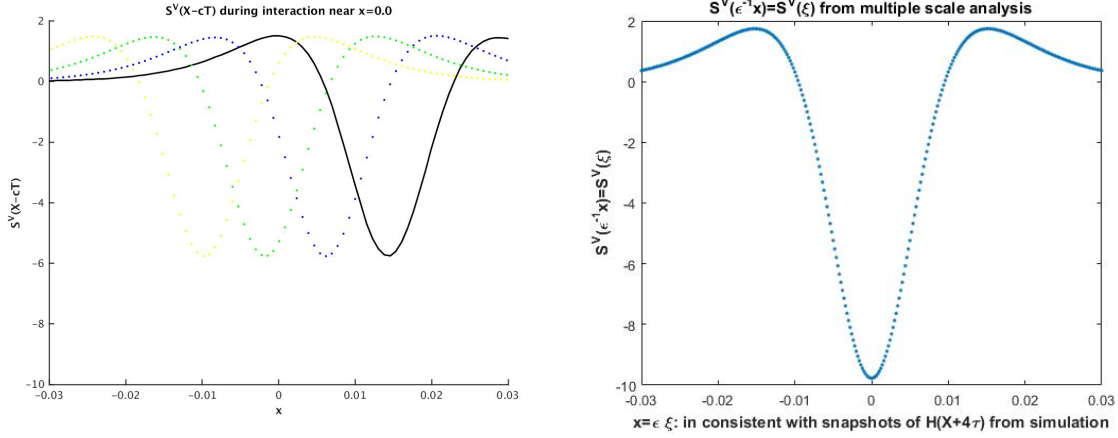


Figure D1. First: $S^V(\xi) = S^V(X - cT)$ at $x \simeq 0$ from simulation with $\epsilon = 10^{-2}$; second: $S^V(\epsilon^{-1}x) = S^V(\xi)$ from multiple scale analysis with $x = \epsilon\xi$ in order to be consistent with $S^V(X - cT)$ from simulation – it is predicted by asymptotic model from (18) and numerically plotted via finite difference method with Cauchy boundary condition $S^V(-10) = S^V(10) = 0$.

Thus, (9a, 9b) can be obtained.

Appendix C. Derivation of right boundary values for H^U and H^V

By taking $\lim_{\xi \rightarrow \infty}$ on both sides of (20), right boundary value of H^U appears as:

$$\begin{aligned} \lim_{\xi \rightarrow \infty} H^U(\xi) &= - \lim_{\xi \rightarrow \infty} \frac{8\sqrt{3}/3 \int_{-\infty}^{\xi} [12 - S^U(\eta)] \operatorname{sech}^2(\eta) d\eta}{4 + 6 \operatorname{sech}^2(\xi)} \\ &= \frac{2\sqrt{3}}{3} \int_{\mathbb{R}} [S^U(\eta) - 12] \operatorname{sech}^2(\eta) d\eta \\ \text{use (16)} \quad &= -\frac{4\sqrt{3}}{9} \int_{\mathbb{R}} S^U(\eta) d\eta. \end{aligned} \quad (\text{C.1})$$

By taking $\lim_{\xi \rightarrow \infty}$ on both sides of (22), right boundary value of H^V appears as:

$$\begin{aligned} \lim_{\xi \rightarrow \infty} H^V(\xi) &= \lim_{\xi \rightarrow \infty} \frac{-8\sqrt{3}/3 \int_{-\infty}^{\xi} [12 - S^U(\eta) + 2S^V(\eta)] \operatorname{sech}^2(\eta) d\eta}{4 - 12 \operatorname{sech}^2(\xi)} \\ &= \frac{2\sqrt{3}}{3} \int_{\mathbb{R}} [S^U(\eta) - 12 - 2S^V(\eta)] \operatorname{sech}^2(\eta) d\eta \\ \text{use (18)} \quad &= -\frac{4\sqrt{3}}{9} \int_{\mathbb{R}} S^V(\eta) d\eta. \end{aligned} \quad (\text{C.2})$$

Appendix D. Observation and verification of V^F

Numerical observation of V^F is quite difficult once realizing $\epsilon^{-2}V^0$ part of wave v is so tall that one could hardly observe its bottom (namely, the area where v obtains $\min v$);

this corresponds to the fact that in the limit of $\epsilon \rightarrow 0$, v wave tends to be singular. Luckily, we can balance the order of ϵ in (3) instead. This reveals V^F is of order $O(\epsilon^0)$.

Again, we can validate our ansatz (5)

$$v(x, t) = \epsilon^{-2}V^0(X, T) + V^F(x, X, T) + \epsilon V^R(x, X, T) + o(\epsilon^0),$$

and corresponding fast-slow decomposition (10b)

$$V^F(x, X, T) = \text{sech}^2(x)S^V(X - cT).$$

Notice from fast-slow decomposition (10b) and ansatz (5), we have

$$\begin{aligned} & \cosh^2(x)V^F(x, X, T) \\ &= \cosh^2(x) \left\{ v(x, X, T) - [\epsilon^{-2}V^0(X - \delta(x, X, T), T) + o(\epsilon^0)] \right\} \\ &= \cosh^2(x) \left\{ v(x, X, T) - \epsilon^{-2}F(X - \delta(x, X, T), T) \right\} + o(\epsilon^0) \end{aligned}$$

where $\delta(x, X, T)(> 0)$ increases as $T(> 0)$ increases and x fixed, since existence of u indeed "delays" KdV movement of v ; by comparison, existence of v indeed "delays" KdV movement of u ; modification of shifts can only be manually made up till now.

Figure D1 shows

- (first) S^V from numerical simulations near $x = 0$ via the numerical method described above and
- (second) S^V predicted by asymptotic model from (18) numerically via finite difference method with Cauchy boundary condition $S^V(-10) = S^V(10) = 0$.

The solitary structure with two small bumps at two sides is evident and is a shared feature for theoretical results and numerical results. However, the integral quantity as well as other feature for exact size of S^V is different. According to (C.2), it is precisely this integral quantity that determines right boundary value for H^V , which is an important feature for H^V . According to (C.2), the inconsistency can be view of ill-prediction of integral quantity of S^V by our asymptotic model.

References

- [1] Biello J A and Majda A J 2005 *Journal of the atmospheric sciences* **62** 1694–1721
- [2] Frierson D M, Majda A J, Pauluis O M et al. 2004 *Communications in Mathematical Sciences* **2** 591–626
- [3] Majda A J and Biello J A 2004 *Proceedings of the National Academy of Sciences of the United States of America* **101** 4736–4741
- [4] Smith R K 2013 *The physics and parameterization of moist atmospheric convection* vol 505 (Springer Science & Business Media)
- [5] Majda A J and Klein R 2003 *Journal of the Atmospheric Sciences* **60** 393–408
- [6] Biello J A and Majda A J 2004 *Studies in Applied Mathematics* **112** 341–390
- [7] Majda A J and Biello J A 2003 *Journal of the atmospheric sciences* **60** 1809–1821
- [8] Majda A J, Rosales R R, Tabak E G and Turner C V 1999 *Journal of the atmospheric sciences* **56** 4118–4133

- [9] Dutrifoy A, Schochet S and Majda A J 2009 *Communications on pure and applied mathematics* **62** 322–333
- [10] Majda A J and Stechmann S N 2009 *Proceedings of the National Academy of Sciences* **106** 8417–8422
- [11] Stechmann S N and Ogrosky H R 2014 *Geophysical Research Letters* **41** 9097–9105
- [12] Stechmann S N and Majda A J 2015 *Monthly Weather Review* **143** 395–416
- [13] Ogrosky H R and Stechmann S N 2015 *Quarterly Journal of the Royal Meteorological Society* **141** 2654–2669
- [14] Ogrosky H R and Stechmann S N 2015 *Journal of the Atmospheric Sciences* **72** 4821–4843
- [15] Harlin J and Majda A J 2013 *Quarterly Journal of the Royal Meteorological Society* **139** 119–136
- [16] Biello J A and Majda A J 2004 *Geophysical & Astrophysical Fluid Dynamics* **98** 85–127
- [17] Khouider B and Majda A J 2005 *Theoretical and Computational Fluid Dynamics* **19** 331–354
- [18] Biello J A 2009 *Chinese Annals of Mathematics, Series B* **30** 483–504
- [19] Ji X, Neelin J D, Lee S K and Mechoso C R 2014 *Journal of Climate* **27** 684–697
- [20] Ji X, Neelin J D and Mechoso C R 2015 *Journal of Climate* **28** 8860–8872
- [21] Raupp C F and Silva Dias P L 2010 *Tellus A* **62** 706–718
- [22] Li J and Titi E S 2015 *arXiv preprint arXiv:1504.05285*
- [23] Bona, Jerry L; Cohen, Jonathan; Wang, Gang 2014 *Nagoya Mathematical Journal* **215**
- [24] Guo Y, Simon K and Titi E S 2013 *arXiv preprint arXiv:1310.1130*
- [25] Krechetnikov R and Marsden J 2009 *Journal of Physics A: Mathematical and Theoretical* **42** 412004
- [26] Vodová-Jahnová J 2015 *Nonlinear Analysis: Real World Applications* **22** 148–154
- [27] Chen S and Stechmann S N 2015 *arXiv preprint arXiv:1510.00880*
- [28] Khouider B, Majda A J and Stechmann S N 2012 *Nonlinearity* **26** R1